Free-Breathing Diffusion Tensor Imaging and Tractography of the Human Heart in Healthy Volunteers Using Wavelet-Based Image Fusion

Hongjiang Wei, Magalie Viallon, Benedicte M. A. Delattre, Kevin Moulin, Feng Yang, Pierre Croisille, and Yuemin Zhu*

***Abstract*—Free-breathing cardiac diffusion tensor imaging (DTI) is a promising but challenging technique for the study of fiber structures of the human heart *in vivo*. This work proposes a clinically compatible and robust technique to provide three-dimensional (3-D) fiber architecture properties of the human heart. To this end, 10 short-axis slices were acquired across the entire heart using a multiple shifted trigger delay (TD) strategy under free breathing conditions. Interscan motion was first corrected automatically using a nonrigid registration method. Then, two post-processing schemes were optimized and compared: an algorithm based on principal component analysis (PCA) filtering and temporal maximum intensity projection (TMIP), and an algorithm that uses the wavelet-based image fusion (WIF) method. The two methods were applied to the registered diffusion-weighted (DW) images to cope with intrascan motion-induced signal loss. The tensor fields were finally calculated, from which fractional anisotropy (FA), mean diffusivity (MD), and 3-D fiber tracts were derived and compared. The results show that the comparison of the FA values ($\mathrm{FA_{PCATMIP}} = 0.45 \pm 0.10, \mathrm{FA_{WIF}} = 0.42 \pm 0.05, \mathrm{P} = 0.06$) showed no significant difference, while the MD values ($\mathrm{MD_{PCATMIP}} = 0.83 \pm 0.12 \times 10^{-3}$ mm^2/s, $\mathrm{MD_{WIF}} = 0.74 \pm 0.05 \times 10^{-3}$ mm^2/s, $\mathrm{P} = 0.028$) were significantly different. Improved helix angle variations through the myocardium wall reflecting the rotation characteristic of cardiac fibers were observed with WIF. This study demonstrates that the combination of multiple shifted TD acquisitions and dedicated post-processing makes it feasible to retrieve *in vivo* cardiac tractographies from free-breathing DTI acquisitions. The substantial improvements were observed using the WIF method instead of the previously published PCATMIP technique.**

***Index Terms*—Diffusion tensor imaging (DTI), fiber architecture, free-breathing, *in vivo* heart.**

I. Introduction

THE HUMAN heart muscle is composed of cardiac myocytes that are 80–100 μm in length and have a cylindrical shape, with a radius of 5–10 μm. These myocytes are branched and are attached to each other by intercalated disks. Therefore, from a microscopic point of view and strictly speaking, the myocardium does not contain so-called fibers as opposed to brain white matter tissue. However, the attached and branched cardiac myocytes form elongated and orientation preference structures and are, for simplicity, often regarded as fibers or bundles of fibers. Diffusion-weighted (DW) magnetic resonance imaging is a valuable technique for probing microscopic structures of biological tissues by measuring changes in the signal due to water molecule diffusion [1]. By acquiring DW images with different diffusion gradient directions (at least six), one can obtain diffusion tensors [i.e., diffusion tensor imaging (DTI)] [2]. DTI has been used to depict fiber architecture properties in *ex vivo* human hearts [3]–[7], in healthy human hearts [8]–[13], and in patients [14]–[17]. Respiratory gated approaches [13], [18] were often preferred to minimize the effect of respiratory motion in DTI acquisitions, although the data can also be obtained from multiple breath-holding acquisitions [18]–[20]. Although more patient friendly, respiratory gated strategies imply increased acquisition time [21] because only 30%–40% of the respiratory cycle [22] is actually used for the acquisitions.

The motivation is high for a 100% duty cycle free-breathing DTI acquisition method that has a high patient compliance rate. The most significant problem for *in vivo* cardiac DTI is the additional and large signal loss as a result of phase modulation due to respiratory and cardiac motions during the diffusion encoding gradients. The first attempt to collect *in vivo* human diffusion data on the heart used a stimulated echo acquisition mode (STEAM) [8]. Cardiac diffusion imaging using STEAM preparation confers the advantage of having a significantly shorter scan time per RR interval (the interval between two ECG R waves), thus reducing the intrascan motion, but inherently doubling the total scan time compared with spin-echo sequences [13] because encoding and decoding must take place in two consecutive cardiac cycles. Using this technique, Reese *et al.* demonstrated the feasibility of mapping fiber orientations quantitatively in human subjects; they found that cardiac DW imaging has a significant sensitivity to myocardial deformation due to the motion. Tseng *et al.* [10] presented a method of obtaining accurate diffusion data by requiring strain-encoded data and defining a "sweet spot" in the cardiac cycle where the net effect of the strain on the observed diffusion approximates zero. Several implementations [8], [9], [13] were used to compensate for motion-induced signal loss, including retrospective navigators and breath-holding, which required acquisition times

Manuscript received July 01, 2014; revised August 29, 2014; accepted August 31, 2014. Date of publication September 10, 2014; date of current version December 24, 2014. This work was supported by the French ANR under ANR-13-MONU-0009-01. *Asterisk indicates corresponding author.*

H. J. Wei, M. Viallon, B. M. A. Delattre, K. Moulin, and P. Croisille are with CREATIS, CNRS UMR 5220, INSERM U1044; INSA Lyon; University of Lyon, 69100 Lyon, France.

F. Yang is with the Department of Biomedical Engineering, Beijing Jiaotong University, Beijing 100044, China.

*Y. Zhu is with CREATIS, CNRS UMR 5220, INSERM U1044; INSA Lyon; University of Lyon, 69100 Lyon, France (e-mail: weihjhit@gmail.com).

Color versions of one or more of the figures in this paper are available online at http://ieeexplore.ieee.org.

Digital Object Identifier 10.1109/TMI.2014.2356792

of approximately 7 min/slice. In the majority of these studies, however, either a single [10], [12], [13] or a group of three [18] slices could be acquired. A 3-D reconstruction of cardiac fiber architecture was proposed using more slices to derive an *in vivo* human atlas through conformal mapping schemes [24]. Nevertheless, neither three [18] nor five [23] slices are ideal for the 3-D fiber architecture reconstruction of the entire heart. The 3-D cardiac fiber architecture construction using a streamline algorithm would benefit from a higher number of slices.

The aim of this study was to investigate the feasibility of *in vivo* cardiac DTI and 3-D fiber tracking of the entire heart under free breathing conditions without any respiratory synchronization. To this end, motion-reduced *in vivo* cardiac DTI datasets were acquired at end-diastole using a multiple shifted trigger delay (TD) acquisition strategy. A nonrigid registration method [31], [32] was used to correct interscan motion. Then, two different postprocessing methods were performed on the multiple TD DW images to compensate for the intrascan signal loss. One is the previously validated PCATMIP method [25], [26], [33], which is based on principal component analysis (PCA) combined with temporal maximum intensity projection (TMIP). Another is a wavelet-based image fusion (WIF) approach combined with the recently developed PCA denoising method [40]. The final corrected DW images were used to calculate the tensor field, from which diffusion parameters, such as fractional anisotropy (FA), mean diffusivity (MD), helix angle (HA), and *in vivo* fiber architecture (3-D fiber tracts), were calculated and compared. The ground-truth simulated data using polarized light imaging (PLI) were also processed using the newly proposed WIF technique and compared with those of PCATMIP.

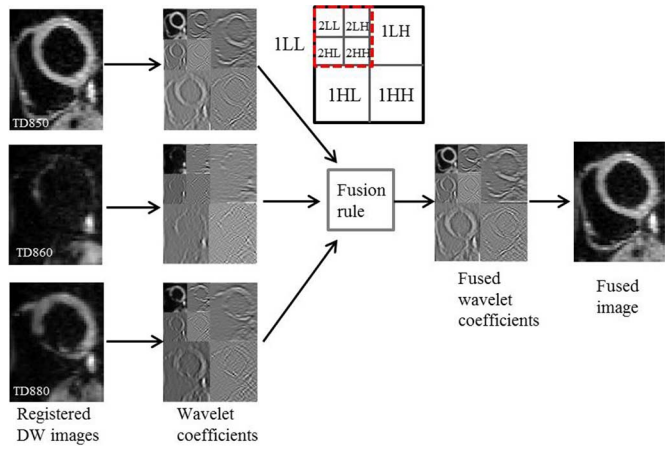

Fig. 1. DW images fusion scheme using the wavelet transform in a two-level decomposition. Wavelet transformed images from the source images include one low-frequency portion (up-left of the multiscale wavelet transformed images) and six high-frequency portions. First level decomposition produces four subbands: 1LL, 1LH, 1HL, and 1HH, which denote the low-low frequency, low-high frequency, high-low frequency, and high-high frequency bands, respectively. The 1LL subband will be the input of the second level decomposition, further resulting in another four subbands (2LL, 2LH, 2HL, and 2HH).

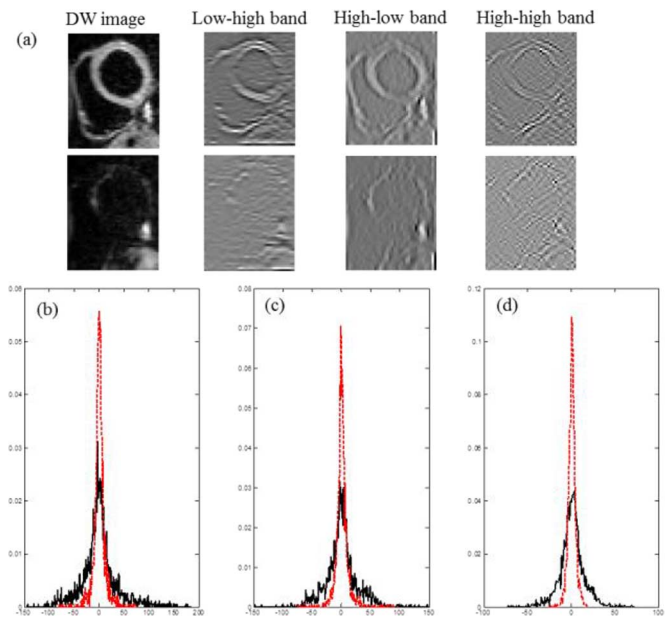

Fig. 2. High-frequency band distribution of wavelet coefficients is different for the DW images exhibiting different motion effects. (a) Two TD images with their high-frequency bands; the top row image is acquired with less motion and the bottom row image with greater motion. (b)–(d) Histograms of the wavelet coefficients of the images that were less influenced by motion (black line) and those of the image that were greatly influenced by motion (red line), respectively. (b) Low-high band. (c) High-low band. (d) High-high band.

II. Materials and Methods

Our method is globally described as below. First, 10 short-axis slices covering the entire heart DW images were acquired with less signal loss at the end of diastole than in the systole [33]. The acquisitions occurred inside an optimal time window using a multiple shifted TD strategy under free breathing conditions. The interscan motion was first corrected automatically using a nonrigid registration method [32]. Then, the WIF method was applied to the registered DW images to cope with intrascan motion-induced signal loss. The noise in the DW images was removed using a state-of-the-art algorithm based on PCA with a local pixel grouping approach [40]. These DW images were then used to calculate the tensor fields. Subsequently, FA, MD, and fiber angles were calculated from the tensor fields. Finally, the 3-D fiber architecture of the human heart was obtained from multi-slice data using the streamline algorithm [46].

A. WIF Processing Scheme

Wavelet fusion techniques [35], [36] are commonly used to combine multiple images into a single image by retaining desired local features in each image and thus providing a more accurate description of the object. In our case, we would like to collect all of the meaningful diffusion information from the input images (multiple TDs) while discarding the parts that were strongly affected by motion. Fig. 1 shows a schematic diagram to better illustrate the concept and procedure of the WIF approach. The basic idea is to perform the multiple scale decomposition on each source image; the transform coefficients of both the low-frequency and high-frequency bands are then fused with a certain pixel-level fusion rule at each scale. The most important aspect in this scheme is the manner of combining the wavelet coefficients. As observed in Fig. 2(b), the high-frequency band distribution is different for the images with different motion artifact levels. More specifically, the spreading

of the wavelet coefficient distribution of the more motion-corrupted image is narrower than that of a less motion-degraded image. That is to say, the image with more motion effects yields more wavelet coefficients that are close to zero and less wavelet coefficients with large magnitudes compared with the images that are less influenced by motion. This motivates us to propose a fusion rule for high-frequency bands. The rule consists of only selecting the information from the high-frequency band yielding a wider spreading distribution. More specifically, for the coefficient to be chosen at location k, we set a $N \times N$ $(N = 5)$ window centered on it for local coefficient statistics. The high-frequency coefficients of the fused image [denoted as $C_F^H(k)$] are produced by combining those of the two source images [denoted as $C_A^H(k)$ and $C_B^H(k)$] as

$$C_F^H(k) = \begin{cases} C_A^H(k), & \text{if } \sigma_A(k) \geq \sigma_B(k) \\ C_B^H(k), & \text{otherwise} \end{cases} \quad (1)$$

where $\sigma_A(k)$ and $\sigma_B(k)$ are the standard deviations (SDs) of the high-frequency coefficients in the window of the two input images, respectively.

The low-frequency wavelet coefficients reflect the global information of the entire image. Normally, signal loss is regional in DW images, and the low-frequency coefficients do not significantly fluctuate. However, at some TDs, the motion can affect the entire heart, thus leading to a decrease in the magnitude of low-frequency coefficients. The low-frequency band represents the signal magnitude of the image; therefore, for each pixel location k, the largest absolute wavelet coefficient was selected among different TDs to avoid signal loss.

By applying the above fusion rule to the wavelet coefficients of each location, we obtained the combined wavelet coefficients. The fused image is then obtained by performing the inverse wavelet transform of the combined wavelet coefficients. In this study, we used Daubechies wavelets with eight vanishing moments, which has been widely used in image fusion [38], [39].

The detailed fusion steps (Fig. 1) are summarized as follows.

Step 1) The multiple TD DW images corresponding to the same diffusion encoding direction are decomposed into wavelet-transformed images (two-level wavelet decomposition using Daubechies wavelets is used to bring out the detailed information in the diffusion-weighted images of the human heart). The transformed images include one low-frequency portion (low-low band) and six high-frequency portions (low-high bands, high-low bands, and high-high bands).

Step 2) The transform coefficients of different bands are fused with the proposed fusion rule.

Step 3) The fused spatial image is obtained by applying the inverse wavelet transform on the fused wavelet coefficients from Step 2.

Step 4) Steps 1–3 are repeated for the DW images in all of the diffusion encoding directions as well as the b0 image (no diffusion weighting).

In vivo cardiac DTI is highly susceptible to noise. The noise, primarily at the level of DW images, can produce errors in the subsequent calculations of diffusion parameters [33], [37]. Thus, after the WIF, removing the noise is crucial for the practical use of DTI for the human heart. We used a state-of-the-art algorithm for denoising images based on PCA with a local pixel grouping approach [40]. More details can be found in [40].

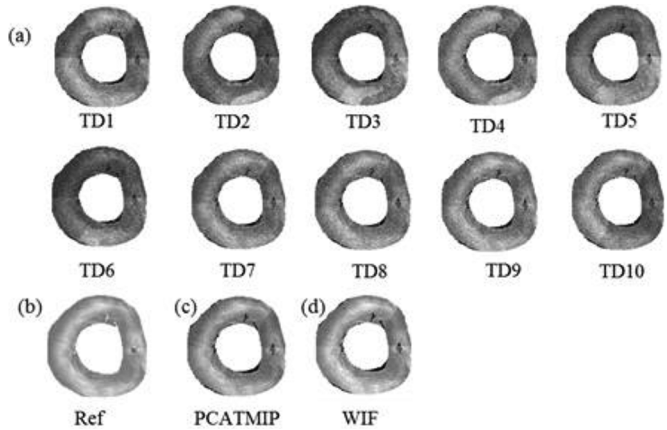

Fig. 3. (a) Simulated 10 TD DW images with cardiac motion. (b) Reference DW image. (c) PCATMIP result. (d) WIF result.

B. Simulation

Simulated data were obtained as proposed in [33]. Briefly, the diffusion behavior of water molecules in the cardiac fiber structure was firstly simulated based on a series of cardiac PLI data using the Monte Carlo method [41]. Simulated DW images were then generated in six directions with b-value $= 2000$ s/mm^2. 43 slices covering the whole heart were simulated from PLI data. Rician noise was added to the simulated DW images to imitate real noise situations. In parallel, an empirical model describing the relationship between cardiac motion and diffusion signal intensity was established by combining the DENSE [47] and DW images acquired at the same time points through the entire cardiac cycle. According to cardiac motion information obtained from DENSE acquisitions and the proposed motion model, the corresponding signal loss was calculated and was added to the simulated DW images to mimick *in vivo* cardiac DW images contaminated with realistic intrascan cardiac motion. A temporal resolution of 10 ms of DENSE encoded data in diastole can be achieved by interpolating from the original acquired DENSE data. Therefore, 10 DW images at 10 TDs in diastole with signal loss caused by cardiac motion were generated for each diffusion encoding direction, which resulted in a total of 60 multiple directional and multiple TD DW images and six reference images with a null diffusion gradient.

The obtained simulated data with added noise and motion artifacts are shown in Fig. 3(a). The 10 TD DW images were hence reconstructed using the above described WIF technique and compared with those of PCATMIP. One direction of the ground-truth data to be compared with is shown in Fig. 3(b). The signal-to-noise ratio (SNR) of the DW images was then defined to assess the quality of the processed DW images from different methods. Diffusion tensor-derived parameters such as FA and MD were also evaluated. The SNR of the DW images was defined by

$$\mathrm{SNR} = \frac{\langle I \rangle_{\mathrm{LV}}}{\mathrm{Noise}} \quad (2)$$

where $\langle I \rangle_{\mathrm{LV}}$ denotes the pixel intensity mean over the left ventricle (LV) wall and "Noise" was measured as the standard deviation (SD) of the pixel intensities over the LV wall.

C. Real Data Acquisitions

Images were acquired on a 1.5T clinical scanner (MAGNETOM Avanto, Siemens AG, Healthcare Sector, Erlangen, Germany) with a maximum gradient strength of 45 mT/m and a maximum slew rate of 200 mT/m/ms. Six healthy volunteers were recruited in this study, including four males and two females with a mean age of 30 ± 9 years (from 25 to 50). For DW image acquisitions, we chose a single-shot twice-refocused spin-echo echo-planar imaging (EPI) sequence with optimized bipolar diffusion encoding gradients [27], improved fat suppression using a gradient reversal technique [28], and standard global phase correction [29]. The twice-refocused spin echo diffusion encoding scheme reduces the impact of eddy current artifacts [34]. All subjects gave informed consent to the institutional review board-approved study protocol prior to participation.

Prior to the diffusion acquisitions, standard 2-chamber, 4-chamber, and short-axis cines were acquired. The time corresponding to minimal motion in diastole was chosen on the short-axis and long-axis views of the cine sequences and was considered as the optimal central time position of the acquisition time window [26], [33] for each multiple-directional and multiple TD diffusion scan. The acquisition window is long enough for the diffusion encoding preparation and the length of the EPI echo train. For each of the 12 gradient directions (diffusion weighting) as well as the b0, 10 shifted acquisitions with increased TD (by 10 ms) were sequentially performed. To cover the entire LV, 10 slices (thickness $= 6$ mm) were acquired in the short-axis view without any interslice gap. These resulted in the acquisition of 1300 DW images and a total scan time of approximately 25 min to cover the entire heart for each volunteer (assuming an average heart rate of 60 beats/min). The localized first- and second-order shimming was performed with an adjustment box fitting the entire heart. Because multiple slice imaging is not realistic with breath-holding scanning due to the high number of breath holds required, all scans were performed under free breathing. The main MRI parameters are as follows: $\mathrm{TE/TR} = 51/100$ ms, spatial resolution $= 2.6 \times 2.6 \times 6$ mm^3, acceleration rate $= 2$ (parallel imaging, GRAPPA), partial Fourier $= 6/8$, matrix size $= 160 \times 90$, FOV $= 420 \times 236$ mm^2, bandwidth $= 1\,302$ Hz, directions $= 12$, and $\mathrm{b} = 200$ s/mm^2.

D. Interscan Motion Correction

Respiratory and cardiac motions affect free-breathing diffusion acquisitions in two ways depending on the nature of the motion with respect to the acquisition time. First, there is the interscan motion corresponding to the movement of the organ during the period between two consecutive diffusion acquisitions. Second, the intrascan motion occurs between each line of k space during the single-shot measurement. The intrascan motion leads to phase-related artifacts that manifest as a severe signal loss of the DW images [30].

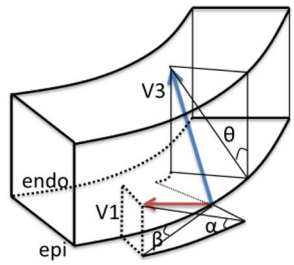

Fig. 4. Definition of helix (α), transverse (β), and sheet (θ) angles with respect to the tensor's primary (V1) and tertiary (V3) eigenvectors.

To correct interscan motion, a fast nonrigid image registration algorithm [31], [32], [50], chosen for its accuracy and reproducibility in noisy cases, was applied to the multiple-directional and multiple TD DW images. The image registration was performed within MATLAB (R2010b, MathWorks, Inc., Natick, MA, USA).

E. Intrascan Motion Correction Using WIF

After interscan motion correction, we applied the PCATMIP [25], [26], [33] and WIF methods to the registered $\mathrm{b} = 200$ TD-shifted DW images with multi-directions and $\mathrm{b} = 0$ images to obtain a unique set of final $\mathrm{b} = 0$ and $\mathrm{b} = 200$ multi-directional motion-corrected DW images.

F. Data Analysis and Quantification of Diffusion Parameters

The image post-processing was performed using MATLAB. The diffusion parameters were measured in the LV after manual segmentation of the myocardium in the b0 image (null diffusion gradient) and the exclusion of the papillary muscles. The diffusion tensor was calculated for each voxel using the signal intensities from the 12 DW images and the b0 image. The eigenvalues and eigenvectors were then obtained for each tensor. Two quantitative diffusion parameter maps were derived from the eigenvalues and eigenvectors: FA and MD [42]. FA is an index of the degree of deviation of the observed diffusion from isotropic or free diffusion, and MD is the first moment of the diffusion tensor, which represents the mean diffusivity. The maximal local diffusion direction, revealed by the primary eigenvector of the diffusion tensor, is along the fiber direction, while the secondary eigenvector is assumed to lie within the laminar sheet. The tertiary eigenvector would be related to the normal of the laminar sheet [48]. The principal eigenvector of the diffusion tensor was taken to represent the mean intravoxel fiber orientation. HA (α in Fig. 4) was computed as the angle between the short-axis plane and the projection of the angle on the tangent plane of the epicardium. Transverse angle (TA) (β in Fig. 4) was computed as the angle between the projection of the fiber in the short-axis plane and tangent plane. The laminar sheet angle (SA) (θ in Fig. 4) is the angle between the plane containing the radial and longitudinal directions and the projection of the tertiary eigenvector in this plane. To improve the tensor field resolution (more exactly, apparent resolution), the diffusion tensors were interpolated in the plane by a factor of 2 using the Log-Euclidean method, which avoids swelling effects [44]. 3-D fiber tracts were constructed by integrating the principal eigenvectors from the diffusion tensor fields using a streamline algo-

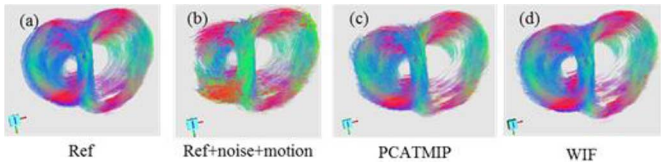

Fig. 5. Fiber tracts derived from (a) simulated reference images, (b) reference +noise+motion images, (c) PCATMIP-processed images, and (d) WIF-processed images. Red, green, and blue colors of the tensors represent the local orientation of the fibers, and indicate left-right-, up-down-, and anterior–posterior-oriented fiber populations, respectively.

rithm. The parameters used for tracking were 0.05 for the FA threshold and 20 voxels for the minimal fiber length [43]. 3-D visualization of the tensors with cylinder glyphs was achieved with medInria (INRIA Sophia-Antipolis, France).

To evaluate different postprocessing methods for *in vivo* cardiac DTI based on the diffusion data acquired at multiple shifted TDs, a comparison was performed between WIF and previously validated PCATMIP methods [33]. The respective FA, MD, HA, and tensor fields were compared. The fiber HA was calculated over five transmural zones of the LV. Finally, the 3-D fiber tracts were constructed and compared.

Differences in diffusion tensor parameters obtained with the two processing methods were assessed using the Wilcoxon signed-rank test. Measurements were presented as the $\text{means} \pm \text{SD}$, and $\text{P} < 0.05$ was considered to be statistically significant. All statistical computations were performed using SPSS 20 (SPSS Inc., Chicago, IL, USA).

III. Results

A. Results on Simulated Data

The DW images [Fig. 3(c) and (d)] corrected using the WIF method offered an overall increased SNR (5.9) compared with the PCATMIP (5.3). Table I provides a quantitative analysis of the impact of cardiac motion on SNR and fiber architecture properties. After processing by the WIF, we observed lower FA values with respect to the PCATMIP (-3%). We also observed smaller MD values with respect to the WIF (-19%). Although the FA and MD values obtained from the WIF were higher than the reference true value, they were much closer to the reference values than those obtained via PCATMIP. Fig. 5(a) shows the ground-truth fiber architecture. The noise and motion strongly impact the fiber structure reconstruction, and the 3-D fiber tracts were completely corrupted by the motion, as shown in Fig. 5(b). The proposed WIF technique enables an efficient correction of the data and further enables one to retrieve the fiber architecture from the artifacted DW images. We can also visually appreciate the superior improvement of the tractography after postprocessing with WIF compared with PCATMIP [Fig. 5(c) and (d)].

B. Results on In Vivo Data

Fig. 6 shows an example of *in vivo* cardiac DW images of a volunteer acquired near the base of the heart. Although the multiple shifted TD acquisitions were collected at end-diastole where in-plane and through-plane heart motion of the LV were minimal, signal intensity fluctuations due to residual cardiac and respiratory motions remain important in the free-breathing acquisitions. Fig. 6(a) shows the registered DW images of the 10 TD acquisitions in a given diffusion gradient direction. TD-specific regional signal losses in the myocardium are clearly visible. Fig. 6(b) shows the DW image obtained after applying the PCATMIP and WIF methods to the 10 TD registered DW images. The combined images exhibit substantially reduced signal loss due to intrascan motion and presented a reduced noise. The combined image obtained using the WIF method had better image quality than that obtained using the PCATMIP method. The DW images [Fig. 6(b)] corrected using the WIF method offered an increased SNR (5.6) compared with those of the PCATMIP (5.08). Significant difference was found between mean $\text{SNR}_{\text{PCATMIP}}$ (5.7) and SNR_{WIF} (5.0) over all the subjects, $\text{P} = 0.04$.

TABLE I
Quantitative Analysis of the Impacts of Cardiac Motion on SNR and Fiber Architecture Properties Using Simulated Data. MD Values Are in Units of 10^{-3} mm^2/s

	SNR	FA ± SD	MD ± SD
Ref	6.8	0.56	0.78
Ref+noise+motion	3.7	0.62 ± 0.10	2.45 ± 1.21
PCATMIP	5.3	0.59 ± 0.02	1.13 ± 0.49
WIF	5.9	0.57 ± 0.01	0.92 ± 0.30

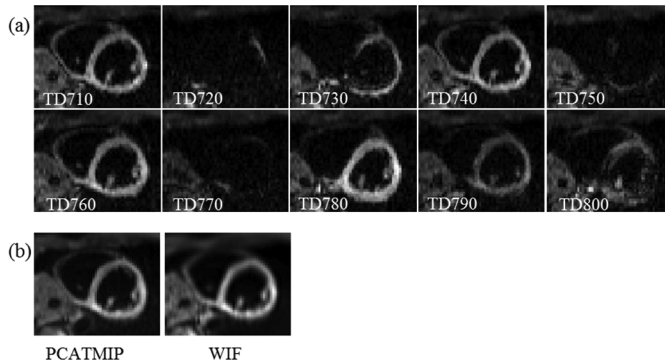

Fig. 6. (a) Free-breathing short-axis DW images resulting from one diffusion acquisition performed at 10 TDs in diastole on a volunteer. Visible spatial signal intensity fluctuation resulting from spatially variable intrascan motion. (b) Corresponding processed DW images using the PCATMIP (left) and WIF (right) methods.

Fig. 7 illustrates the FA and MD maps of a volunteer. The mean FA and MD values in each volunteer and the mean values from all of the volunteers are given in Fig. 8(a) and (b). Both the FA and MD values were defined as the mean values over the 10 slices of each subject. The global $\text{FA}_{\text{PCATMIP}}$ (0.45 ± 0.10) was higher than FA_{WIF} (0.42 ± 0.05). No significant difference was found between FA values $(\text{P} = 0.06)$. MD_{WIF} $(0.74 \pm 0.05 \times 10^{-3}$ mm^2/s) was significantly lower than $\text{MD}_{\text{PCATMIP}}$ $(0.83 \pm 0.12 \times 10^{-3}$ mm^2/s), $\text{P} = 0.028$.

The means ±SD of the HA values in the five layers for all of the volunteers are shown in Fig. 9(a). With PCATMIP, the mean HAs varied from $28^\circ \pm 13^\circ$ in the endocardium layer, through $24^\circ \pm 5^\circ$ in the mid-endocardium layer and $13^\circ \pm 5^\circ$ in the mid-wall, and $-7^\circ \pm 7^\circ$ in the mid-epicardium layer to $-27^\circ \pm 7^\circ$ in the epicardium layer. With WIF, the mean HAs varied from $35^\circ \pm 9^\circ$ in the endocardium layer, $22^\circ \pm 6^\circ$ in the mid-endocardium layer and $8^\circ \pm 7^\circ$ in the mid-wall, and

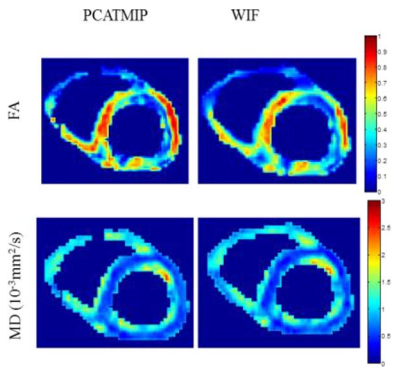

Fig. 7. Examples of FA and MD maps derived using the PCATMIP and WIF methods. Left: PCATMIP. Right: WIF.

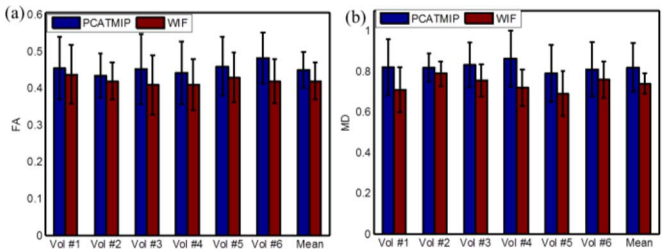

Fig. 8. FA and MD values (means±SD) in each subject and mean values from all of the volunteers obtained using the two methods. (a) FA values in the LVs. (b) MD values in the LVs. MD values are in units of 10^{-3} mm^2/s.

$-14^\circ \pm 6^\circ$ in the mid-epicardium layer to $-31^\circ \pm 7^\circ$ in the epicardium layer. The negative-to-positive angles of the fibers when moving from the epicardiaum to endocardium are an important characteristic of the human cardiac fiber architecture, as described in [45]. The mean TAs obtained from PCATMIP were $17^\circ \pm 13^\circ$, $19^\circ \pm 11^\circ$, $14^\circ \pm 12^\circ$, $6^\circ \pm 8^\circ$, and $-3^\circ \pm 10^\circ$ in the endocardium layer, the mid-endocardium layer, the mid-wall, the mid-epicardium layer, and the epicardium layer, respectively. With WIF, the mean TAs were $-3^\circ \pm 15^\circ$ in the endocardium layer, $-5^\circ \pm 13^\circ$ in the mid-endocardium layer, $-3^\circ \pm 17^\circ$ in the mid-wall, $-1^\circ \pm 11^\circ$ in the mid-epicardium layer, and $-6^\circ \pm 14^\circ$ in the epicardium layer. The comparison on TAs was performed on each layer between PCATMIP and WIF, with $\mathrm{P} < 0.01, \mathrm{P} < 0.01, \mathrm{P} < 0.01, \mathrm{P} = 0.04$, and $\mathrm{P} = 0.02$ for the endocardium, mid-endocardium, mid-wall, mid-epicardium, and epicardium layers, respectively. The mean SAs obtained from PCATMIP were $-6^\circ \pm 11^\circ$, $3^\circ \pm 10^\circ$, $6^\circ \pm 12^\circ$, $5^\circ \pm 7^\circ$, and $-2^\circ \pm 11^\circ$ for the five layers from endocardium to epicardium. With WIF, the mean SAs were $-13^\circ \pm 8^\circ$ in the endocardium layer, $-8^\circ \pm 10^\circ$ in the mid-endocardium layer, $-10^\circ \pm 9^\circ$ in the mid-wall, $-5^\circ \pm 11^\circ$ in the mid-epicardium layer, and $-9^\circ \pm 12^\circ$ in the epicardium layer. No statistically significant differences were found for the SA values between PCATMIP and WIF with $\mathrm{P} = 0.26, \mathrm{P} = 0.65, \mathrm{P} = 0.3, \mathrm{P} = 0.07$, and $\mathrm{P} = 0.09$ for the five layers from endocardium to epicardium. The transverse angle shows a stable mean value of zero along the transmural depth [Fig. 9(b)]. This indicates that fibers are mostly oriented parallel to the wall surface. The sheet angle does not appear to have a significant correlation with the transmural depth [Fig. 9(c)]. Similar results were obtained in a previous study [49]. The HA diagrams

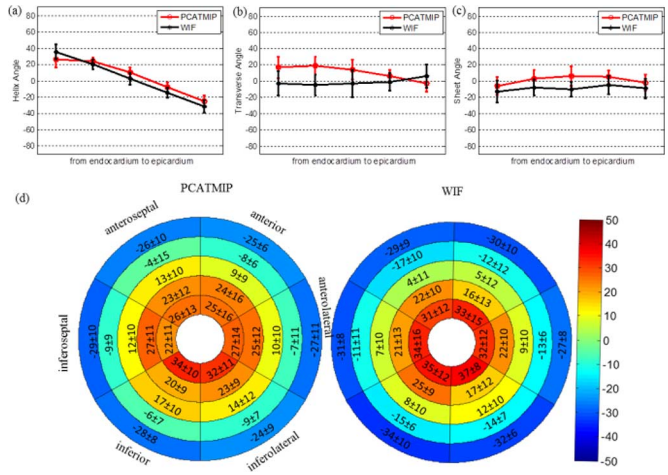

Fig. 9. Helix angle, transverse angle, and sheet angle distributions in LV. (a)–(c) Plots of the helix angle, transverse angle, and sheet angle with respect to the transmural positions from the endocardium to the epicardium. (d) Diagrams of the means±SD of the helix angles. The diagrams depict the different regions (anterior, anterolateral, inferolateral, inferior, inferoseptal, and anteroseptal), which are further equally divided into five layers across the left ventricle.

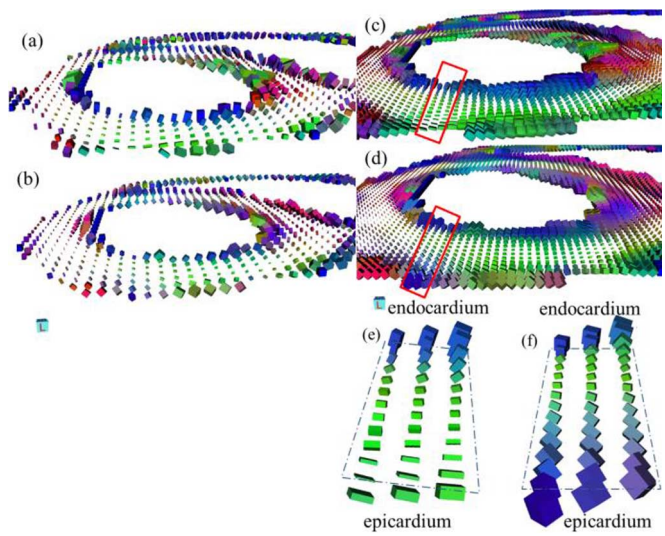

Fig. 10. 3-D visualization of tensor fields using superquadric glyphs derived using the (a), (c) PCATMIP and (b), (d) WIF methods. (a) and (b) Original tensor fields without interpolation. (c) and (d) Tensor fields after interpolating from (a) and (b), respectively. Helical pattern of the cardiac fiber orientations is clearly depicted by the principal eigenvector. (e) and (f) Tensors zoomed from the ROIs in (c) and (d), respectively. Red, green, and blue colors of the tensors represent the local orientation of the fibers, which indicate anterior-posterior-, left-right-, and up-down-oriented fiber populations, respectively.

based on AHA segmentation are furthermore depicted in Fig. 9(d). No statistically significant differences were found when comparing six different regions (anterior, anterolateral, inferior, inferolateral, inferoseptal, anteroseptal) in the same layer either for PCATMIP or for WIF ($\mathrm{P} > 0.05$). The HA values in the WIF and PCATMIP studies show differences in some regions ($\mathrm{P}_{\mathrm{anterior}} = 0.02, \mathrm{P}_{\mathrm{anterolateral}} = 0.78$, $\mathrm{P}_{\mathrm{inferolateral}} = 0.27, \mathrm{P}_{\mathrm{inferior}} = 0.89$, $\mathrm{P}_{\mathrm{inferoseptal}} = 0.065$, and $\mathrm{P}_{\mathrm{anteroseptal}} = 0.053$).

The tensor fields derived from the two methods are shown in Fig. 10. Globally, the helical structures of cardiac fibers can be observed from both PCATMIP [Fig. 10(a) and (c)] and WIF

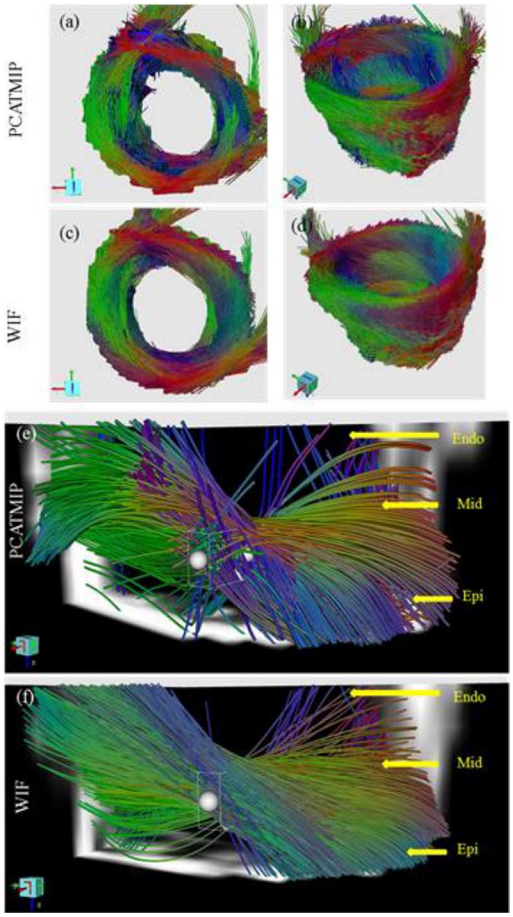

Fig. 11. *In vivo* 3-D fiber tracts of a volunteer derived using the PCATMIP [(a), (b), (e)] and WIF [(c), (d), (f)] methods. The red, green, and blue colors of the tracked fibers indicate the x, y, and z components of the local orientation of the fiber, respectively.

[Fig. 10(b) and (d)] methods. The orientation of the tensors changed uniformly, as indicated by their colors varying from purple on the lateral wall to green on the inferior wall. However, in the subendocardial and subepicardial layers, the tensors provided via PCATMIP were noisier, as indicated by the arrows in Fig. 10(a). WIF with noise removal produced homogeneous tensors [Fig. 10(b)]. The transmural variation was visible in the LV by zooming in on a ROI (region of interest). The orientations of the tensors clearly show the distributions of positive angles on the endocardium and negative angles on the epicardium via the WIF method [Fig. 10(f)]. The improvement due to WIF can be more clearly observed by comparing Fig. 10(e) with (f).

Finally, the examples of *in vivo* 3-D fiber architecture are presented in Fig. 11. The fiber orientations of the LV show a circularly symmetric pattern viewed from the top of the heart [Fig. 11(a) and (c)]. For a better depiction of the helical structure, a shutter located at the lateral wall viewed from the epicardial surface is shown in Fig. 11(e) and (f). Fibers in the endocardium track from the posterior base to the anterior apex, while those in the epicardium track from the anterior base to the posterior apex. Myofibers in the mid-myocardium have zero HA. The regular changes in the fiber orientations in the shutter can be better observed using WIF compared with PCATMIP. The fiber tracking results in the shutter of the same ROI are assessed

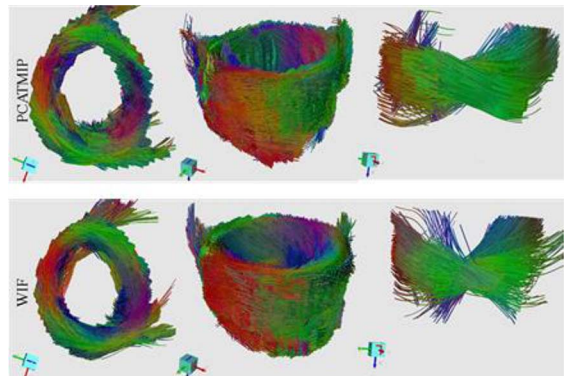

Fig. 12. *In vivo* 3-D fiber tracts of another volunteer derived using the PCATMIP (top) and WIF (bottom) methods.

TABLE II
QUANTITATIVE ANALYSIS OF CARDIAC FIBER IN THE SAME ROI OBTAINED USING THE PCATMIP AND WIF METHODS. THE UNIT OF THE FIBER LENGTH IS IN MILLIMETERS. SD MEANS STANDARD DEVIATION

	Fiber length (number of connecting voxels)			
	max	number	mean	SD
PCATMIP	115	1,332	42	16
WIF	155	2,230	51	14

in terms of the length and the number of fibers, which are presented in Table II. The results show that the maximum and mean fiber lengths are found to be greater via the WIF method than those obtained via PCATMIP. Fig. 12 presents the fiber architecture of the second volunteer. Again, we can recognize the main helical structure of the LV. The WIF method always provided more continuous fiber tracts than the PCATMIP method in any given view of the heart. The obtained fiber tracts were strongly consistent with what we know from an *ex vivo* cardiac DTI study [7].

IV. DISCUSSION

This study investigated *in vivo* human cardiac DTI under free breathing using different postprocessing methods. The multiple shifted TD acquisitions combined with postprocessing enabled us to obtain a coherent fiber tractography of the entire heart. The HA distribution was consistent with the helical structure of myocardial fibers [7], [14], [17], [18]. The results demonstrate the capacity of the PCATMIP and WIF methods to preserve the integrity of the directional information contained in the multiple-directional DW image acquisitions. WIF combined with the denoising method provides more accurate fiber tractography than PCATMIP as shown in simulations and more continuous fiber tracts than PCATMIP performed on *in vivo* data.

The data were acquired on a 1.5T clinical scanner, and the b value of 200 s/mm^2 was selected. Although this value is lower than that used in the literature [13], [14], [16], [18], it was sufficient to reveal the diffusion anisotropy in the myocardium. Using the twice-refocused spin echo sequence, the SNR was too low for b values >200, and this value was chosen as the best compromise in terms of SNR on our 1.5T scanner using this sequence. Some contamination from perfusion to the apparent diffusion coefficient (ADC) cannot be excluded even though the values obtained for MD are consistent with the values obtained

by others [17], [18], [20]. The b values should ideally be increased, especially in patients, where perfusion modifications or inflammatory processes frequently occur and induce regional variations. Improvements in the system hardware and especially the gradient strength should soon enable the use of higher b values at a markedly reduced TE.

The *in vivo* diffusion data acquired at end-diastole has a limited spatial resolution. In principle, (physical) spatial resolution is fixed once the image acquired. Nevertheless, we used interpolation to improve the apparent spatial resolution of DTI data. Although the used Log-Euclidean diffusion tensor interpolation [44] does not increase the true spatial resolution, after interpolation, classical fiber architectures were clearly obtained in our volunteers.

In vivo DTI of the human heart is challenging due to motion and the intrinsically low SNR of the DW images. The central challenge of *in vivo* cardiac DTI is signal loss as a result of phase modulation due to motion during the diffusion encoding gradients. While some approaches have used dedicated MRI sequences to compensate for physiological motion [10], [13], our approach differs from these in that it uses DW sequences available on clinical scanners and acquires data over multiple shifted TD acquisitions in diastole. A previous study [33] demonstrated that signal loss can be minimized in a short systole window as well as in end-diastole. However, the heart motion is heterogeneous, and the bulk motion-induced signal loss is spatially variable and time-dependent. It is therefore difficult to correctly obtain true diffusion information by repeating the acquisitions at the same TD, and it is statistically more efficient to use the multiple shifted TD acquisitions to maximize the chance to collect a motion-free signal. Our results showed that signal loss due to cardiac motion can be, to some extent, overcome through the combination of a dedicated acquisition strategy and adequate postprocessing methods. Our study showed that both PCATMIP and WIF permitted the recovery of DW signal intensities while preserving directional diffusion information; however, more accurate results were obtained with WIF.

Although the multiple shifted TD acquisitions were collected at end-diastole where in-plane and through-plane heart motions of the LV were minimal, the cardiac and respiratory motions could not be completely eliminated due to free-breathing acquisitions. Even small differences in respiratory position due to motion cause significant image misregistration. Image registration is mandatory to correct for interscan motion and is a key step in ensuring geometrical consistency among different directions and TD per slice. It is by design only capable of correcting for in-plane motion and cannot compensate for larger through-plane motion. In our study, the cardiac DTI images were acquired at different time points in a predefined time window. This time window was always during mid- to end-diastole and corresponded to minimal motion (in-plane and through-plane) of the left ventricle on the short-axis and long-axis cine sequences. Despite the residual through-plane motion, we obtain significant 3-D fiber architectures from the *in vivo* data with free-breathing conditions. The results are also in coherence with previous studies [17], [18], [20], [48]. However, the residual motion can contaminate cardiac DTI measurements and could result in some loss of tensor field coherence between slices. Additionally, the streamline tracking by integrating the principal eigenvectors from tensor fields could produce errors in fiber structure construction. We can observe that the 3-D fibers in Fig. 11(b) are sometimes discontinuous in some part of the LV; this is because the principal eigenvectors in these regions are so incoherent or sparse that it is very difficult to correctly track the fibers. This is especially obvious near the apex. Correcting through-plane motion during data acquisitions remains an important topic of further investigation.

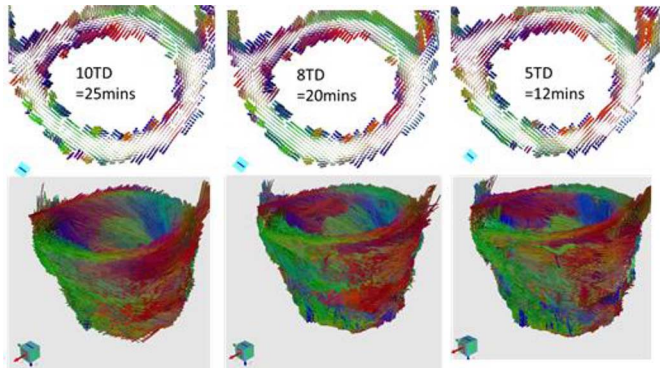

Fig. 13. Comparison of tensor fields and fiber tractographies obtained from a reduced number of TDs.

The number of TDs used in this study, 10, was an approximate number and a good compromise between the acquisition time and the robustness of fiber quality given motion. Reconstruction using a reduced number of TDs was possible in some volunteers, but most of the time, the reduced number of TDs results in the degradation of the tensor field and fiber tractography quality, as illustrated below (Fig. 13). Therefore, fewer acquisitions will not produce the same accuracy. However, the number of acquisitions per direction is a limiting factor for the scan time and an important aspect to be improved in the future.

In this work, we adopted two image combination approaches that enabled us to fuse registered DW images acquired at different TDs. PCATMIP provides high SNR by selecting the highest signal intensity from the input images, while WIF splits the image into sub-images of low- and high-frequencies, which enables us to collect desired features from each decomposed image and combine them using an appropriate fusion rule. Our study showed that selecting wavelet coefficients following the proposed fusion rule can preserve meaningful diffusion information. After further applying a noise removal method, this processing scheme can reconstruct a more accurate helical myofiber pattern than PCATMIP.

Despite the motion and noise difficulties in DTI, the cardiac fiber structure we obtained is consistent with previous *ex vivo* [7] and *in vivo* [18], [24], [48] studies. The mean FA ($\mathrm{FA_{PCATMIP}} = 0.45 \pm 0.10, \mathrm{FA_{WIF}} = 0.42 \pm 0.05$) and MD ($\mathrm{MD_{PCATMIP}} = 0.83 \pm 0.12 \times 10^{-3}$ mm^2/s, $\mathrm{MD_{WIF}} = 0.74 \pm 0.05 \times 10^{-3}$ mm^2/s) are similar to those of previous studies (0.60 ± 0.04 and $0.8 \pm 0.2 \times 10^{-3}$ mm^2/s for breath-holding acquisitions and 0.60 ± 0.03 and $0.9 \pm 0.2 \times 10^{-3}$ mm^2/s for navigator acquisitions) in healthy volunteers [18] via 3T scanner. The previous study on accelerating cardiac DTI using simultaneous multislice

imaging has also shown a similar FA (0.48 ± 0.08) and MD $(1.19 \pm 0.10 \times 10^{-3}$ mm^2/s) values [20]. It should be noted that the quantitative results in the present study were relative to the acquisitions at end-diastole. We may consider differences between the data acquired at different cardiac phases. Although not yet well understood, the fiber architecture of the human heart is dynamically reorganized during the cardiac cycle in relation to the myocardial strain. Furthermore, the WIF method provides lower FA and MD values than PCATMIP, which is strongly consistent with our previous study [33]. The higher MD value in the epicardium and endocardium borders may be due to free-breathing artifacts or a segmentation issue. The HA range obtained in the present study is approximately from 41° on the endocardium to -34° on the epicardium for PCATMIP and from 44° to -38° for the WIF method. The WIF method gives a wider HA range that is more in agreement with *ex vivo* literature [7]. The study reported in [18] of healthy *in vivo* human hearts showed ranges of HA variations from $22^\circ \pm 10^\circ$ on the endocardium to $-17^\circ \pm 6^\circ$ on the epicardium for the breath-holding study and from $7^\circ \pm 7^\circ$ on the endocardium to $-14^\circ \pm 6^\circ$ on the epicardium for a navigated acquisition free-breathing study. The HA distribution of the study [48] on healthy *in vivo* human hearts vary from approximately 55° on the endocardium to approximately -30° on the epicardium for free breathing using a respiratory navigator. The HA ranges obtained using the WIF method are slightly narrower than those in a previous *ex vivo* human cardiac study (HA variations from $66^\circ \pm 15^\circ$ on the endocardium to $-41^\circ \pm 26^\circ$ on the epicardium) [7]. We should consider many factors that may influence HA range, such as *in vivo* and *ex vivo* data, data acquired at different cardiac phases, spatial resolution, and motion artifacts. The segmentation algorithm used to extract the HA values in each layer imposes averaging and may also be responsible for the narrower HA range. Comparing different segmentation algorithms to extract robust quantitative HA data will be a very important issue for future cardiac DTI in clinics.

For the *in vivo* data, significant differences were found for the TA values between PCATMIP and WIF with $\mathrm{P} < 0.01, \mathrm{P} < 0.01, \mathrm{P} < 0.01, \mathrm{P} = 0.04$, and $\mathrm{P} = 0.02$ for the endocardium, mid-endocardium, mid-wall, mid-epicardium, and epicardium layers, respectively. No statistically significant differences were found for the SA values between PCATMIP and WIF with $\mathrm{P} = 0.26, \mathrm{P} = 0.65, \mathrm{P} = 0.3, \mathrm{P} = 0.07$, and $\mathrm{P} = 0.09$ for the five layers, respectively. The differences in TA or SA between PCATMIP and WIF were also observed with simulated data. The TA values obtained from the simulated data for PCATMIP were $6^\circ \pm 6^\circ, 8^\circ \pm 10^\circ, 10^\circ \pm 11^\circ, -5^\circ \pm 8^\circ$, and $-2^\circ \pm 7^\circ$ in the endocardium layer, mid-endocardium, mid-wall, mid-epicardium, and epicardium layers, respectively. The TA values were $4^\circ \pm 5^\circ, 5^\circ \pm 3^\circ, -1^\circ \pm 6^\circ, -3^\circ \pm 6^\circ$, and $-4^\circ \pm 6^\circ$ for WIF. The comparison on TAs was performed on each layer between PCATMIP and WIF showing significant differences with $\mathrm{P} < 0.01, \mathrm{P} < 0.01, \mathrm{P} < 0.01, \mathrm{P} = 0.05$, and $\mathrm{P} = 0.04$ for the five layers, respectively. The SA values obtained from PCATMIP were $8^\circ \pm 9^\circ, -6^\circ \pm 11^\circ, 3^\circ \pm 13^\circ, 6^\circ \pm 7^\circ$, and $7^\circ \pm 10^\circ$ for the five layers, respectively. With WIF, the mean SAs were $10^\circ \pm 5^\circ$ in the endocardium layer, $9^\circ \pm 7^\circ$ in the mid-endocardium layer, $-10^\circ \pm 9^\circ$ in the mid-wall, $-5^\circ \pm 11^\circ$ in the mid-epicardium layer, and $-9^\circ \pm 12^\circ$ in the epicardium layer. The comparison on SAs between PCATMIP and WIF was also performed on the five layers showing no statistically significant differences with $\mathrm{P} = 0.51, \mathrm{P} = 0.25, \mathrm{P} = 0.38, \mathrm{P} = 0.80$ and $\mathrm{P} = 0.76$, respectively. In the absence of ground truth, the results obtained from the simulated data are of crucial importance. The TA obtained from WIF shows a stable mean value of zero along the transmural depth [Fig. 9(b)]. This indicates that fibers are mostly oriented parallel to the wall surface. Similar results were obtained in a previous study [49]. The TA variation across the heart wall suggests that WIF would be more robust than PCATMIP for fiber tracking applications. Further work is needed to know whether the proposed WIF is also able to preserve small pathological structural information while improving tractography quality.

These preliminary experiments demonstrate that the proposed approach (a dedicated acquisition method combined with advanced postprocessing) has the potential to accommodate physiological motion. Although the reproducibility of this work must be evaluated, the proposed approach is feasible for showing *in vivo* fiber structures of the normal heart and may have important implications for the *in vivo* study of heart fiber structures in various diseases. The proposed approach does not require reliable navigator synchronization and could be easy to implement. The acquisition of multiple TD datasets leads to a total scan time of approximately 25 min for each volunteer, which is slightly higher than the acceptable acquisition time scale for clinical applications. The influence of the number of TD shifts needed to provide reliable results should also be investigated. Future work will then concentrate on investigating this aspect in an attempt to minimize the number of TD shifts and in turn further reduce the total scan duration.

V. Conclusion

This work demonstrated that *in vivo* human cardiac DTI with free breathing is feasible in an acceptable scan time. The combination of a multiple shifted TD acquisition strategy and adequate postprocessing methods has the potential to enhance our understanding of *in vivo* cardiac fiber structures. To our best knowledge, this is the first comparison study on the reconstruction of the entire human heart fiber architecture with free-breathing acquisitions using different processing methods. The obtained HA maps indicate the myocardial fiber orientation of the LV, which shows a circularly symmetric pattern from approximately 41° on the endocardium to -34° on the epicardium for PCATMIP and from 44° to -38° for WIF. The TA variation across the LV from WIF indicates that fibers are mostly oriented parallel to the wall surface. The fiber tractographies provided via WIF are more continuous than those obtained using PCATMIP, which suggests that the WIF processing scheme is superior for retrieving diffusion information.

Acknowledgment

The authors thank T. Feweier from Siemens AG, Healthcare Sector, Erlangen, Germany for the advanced diffusion prototype sequence delivery. The authors are also grateful to Prof. P.-S. Jouk, Dr. Y. Usson and G. Michalowicz from the The

TIMC-IMAG laboratory and the Service de Medecine Néonatale, Centre Hospitalier Universitaire de Grenoble, Université Joseph Fourier, Grenoble, France for their assistance with the PLI experiments. The authors thank Dr. L. Wang for the simulated diffusion data from the original PLI images."

REFERENCES

[1] D. Le Bihan, "Molecular diffusion, tissue microdynamics and microstructure," *NMR Biomed.*, vol. 8, no. 8, pp. 375–386, 1995.

[2] P. J. Basser, J. Mattiello, and D. Le Bihan, "Estimation of the effective self-diffusion tensor from the NMR spin echo," *J. Magn. Reson. B*, vol. 103, no. 3, pp. 247–254, 1994.

[3] G. Seemann, D. Keller, and D. L. Weiss, "Modeling human ventricular geometry and fiber orientation based on diffusion tensor MRI," *Comput. Cardiol.*, pp. 801–804, Sep. 2006.

[4] D. Rohmer, A. Sitek, and G. T. Gullberg, "Reconstruction and visualization of fiber and laminar structure in the normal human heart from ex vivo diffusion tensor magnetic resonance imaging (DTMRI) data," *Invest. Radiol.*, vol. 42, no. 11, pp. 777–789, 2007.

[5] C. Frindel, M. Robini, P. Croisille, and Y. M. Zhu, "Comparison of regularization methods for human cardiac diffusion tensor MRI," *Med. Image Anal.*, vol. 13, no. 3, pp. 405–418, 2009.

[6] F. Yang, Y. M. Zhu, I. E. Magnin, J. H. Luo, P. Croisille, and P. B. Kingsley, "Feature-based interpolation of diffusion tensor fields and application to human cardiac DT-MRI," *Med. Image Anal.*, vol. 16, no. 2, pp. 459–481, 2012.

[7] H. Lombaert, J. Peyrat, P. Croisille, S. Rapacchi, L. Fanton, F. Cheriet, P. Clarysse, I. Magnin, H. Delingette, and N. Ayache, "Human atlas of the cardiac fiber architecture: Study on a healthy population," *IEEE Trans. Med. Imag.*, vol. 31, no. 7, pp. 1436–1447, Jul. 2012.

[8] R. R. Edelman, J. Gaa, V. J. Wedeen, E. Loh, J. M. Hare, P. Prasad, and W. Li, "In vivo measurement of water diffusion in the human heart," *Magn. Reson. Med.*, vol. 32, no. 3, pp. 423–428, 1994.

[9] T. G. Reese, R. M. Weisskoff, R. N. Smith, B. R. Rosen, R. E. Dinsmore, and V. J. Wedeen, "Imaging myocardial fiber architecture in vivo with magnetic resonance," *Magn. Reson. Med.*, vol. 34, no. 6, pp. 786–791, 1995.

[10] W. Y. Tseng, T. G. Reese, R. M. Weisskoff, and V. J. Wedeen, "Cardiac diffusion tensor MRI in vivo without strain correction," *Magn. Reson. Med.*, vol. 42, no. 2, pp. 393–403, 1999.

[11] W. Y. Tseng, T. G. Reese, R. M. Weisskoff, T. J. Brady, and V. J. Wedeen, "Myocardial fiber shortening in humans: Initial results of MR Imaging," *Radiology*, vol. 216, no. 1, pp. 128–139, 2000.

[12] J. Dou, T. G. Reese, W. Y. Tseng, and V. J. Wedeen, "Cardiac diffusion MRI without motion effects," *Magn. Reson. Med.*, vol. 48, no. 1, pp. 105–114, 2002.

[13] U. Gamper, P. Boesiger, and S. Kozerke, "Diffusion imaging of the in vivo heart using spin echoes-considerations on bulk motion sensitivity," *Magn. Reson. Med.*, vol. 57, no. 2, pp. 331–337, 2007.

[14] M. T. Wu, W. Y. Tseng, M. Y. Su, C. P. Liu, K. R. Chiou, V. J. Wedeen, T. G. Reese, and C. F. Yang, "Diffusion tensor magnetic resonance imaging mapping the fiber architecture remodeling in human myocardium after infarction," *Circulation*, vol. 114, no. 10, pp. 1036–1045, 2006.

[15] W. Y. Tseng, J. Dou, T. G. Reese, and V. J. Wedeen, "Imaging myocardial fiber disarray and intramural strain hypokinesis in hypertrophic cardiomyopathy with MRI," *J. Magn. Reson. Imag.*, vol. 23, no. 1, pp. 1–8, 2006.

[16] M. T. Wu, M. Y. Su, Y. L. Huang, K. R. Chiou, P. Yang, H. B. Pan, T. G. Reese, V. J. Wedeen, and W. Y. Tseng, "Sequential changes of myocardial microstructure in patients postmyocardial infarction by diffusion-tensor cardiac MR: Correlation with left ventricular structure and function," *Circ. Cardiovasc. Imag.*, vol. 2, no. 1, pp. 32–40, 2009.

[17] L. A. McGill, T. F. Ismail, S. Nielles-Vallespin, P. Ferreira, A. D. Scott, M. Roughton, P. J. Kilner, S. Y. Ho, K. P. McCarthy, P. D. Gatehouse, R. de Silva, P. Speier, T. Feiweier, C. Mekkaoui, D. E. Sosnovik, S. K. Prasad, D. N. Firmin, and D. J. Pennell, "Reproducibility of in-vivo diffusion tensor cardiovascular magnetic resonance in hypertrophic cardiomyopathy," *J. Cardiovasc. Magn. Reson.*, vol. 15, no. 1, pp. 14–86, 2012.

[18] S. Nielles-Vallespin, C. Mekkaoui, P. Gatehouse, T. G. Reese, J. Keegan, P. F. Ferreira, S. Collins, P. Speier, T. Feiweier, R. de Silva, M. P. Jackowski, D. J. Pennell, D. E. Sosnovik, and D. Firmin, "In vivo diffusion tensor MRI of the human heart: Reproducibility of breath-hold and navigator-based approaches," *Magn. Reson. Med.*, vol. 70, no. 2, pp. 454–465, 2012.

[19] B. M. Delattre, M. Viallon, H. Wei, Y. M. Zhu, T. Feiweier, V. M. Pai, H. Wen, and P. Croisille, "In vivo cardiac diffusion-weighted magnetic resonance imaging: Quantification of normal perfusion and diffusion coefficients with intravoxel incoherent motion imaging," *Invest. Radiol.*, vol. 47, pp. 662–670, 2012.

[20] A. Z. Lau, E. M. Tunnicliffe, R. Frost, P. J. Koopmans, D. J. Tyler, and M. D. Robson, "Accelerated human cardiac diffusion tensor imaging using simultaneous multislice imaging," *Magn. Reson. Med.*, 2014.

[21] R. L. Ehman, M. T. McNamara, M. Pallack, H. Hricak, and C. B. Higgins, "Magnetic resonance imaging with respiratory gating: Techniques and advantages," *Am. J. Roentgenol.*, vol. 143, no. 6, pp. 1175–1182, 1984.

[22] P. Summers, P. Staempfli, T. Jaermann, S. Kwiecinski, and S. Kollias, "A preliminary study of the effects of trigger timing on diffusion tensor imaging of the human spinal cord," *Am. J. Neuroradiol.*, vol. 27, no. 9, pp. 1952–1961, 2006.

[23] C. T. Stoeck, T. Nicolas, and B. Peter, "Dual heart-phase cardiac DTI using local-look STEAM," ISMRM Abstract 2012, vol. 10, p. 1.

[24] N. Toussaint, M. Sermesant, C. T. Stoeck, S. Kozerke, and P. G. Batchelor, "In vivo human 3-D cardiac fibre architecture: Reconstruction using curvilinear interpolation of diffusion tensor images," *Med. Image Comput. Comput. Assist. Interv.*, vol. 13, pp. 418–425, 2010.

[25] V. M. Pai, S. Rapacchi, P. Kellman, P. Croisille, and H. Wen, "PCATMIP: Enhancing signal intensity in diffusion-weighted magnetic resonance imaging," *Magn. Reson. Med.*, vol. 65, no. 6, pp. 1611–1619, 2011.

[26] S. Rapacchi, H. Wen, M. Viallon, D. Grenier, P. Kellman, P. Croisille, and V. M. Pai, "Low b-value diffusion-weighted cardiac magnetic resonance imaging: Initial results in humans using an optimal time-window imaging approach," *Invest. Radiol.*, vol. 46, no. 12, pp. 751–758, 2011.

[27] T. Feiweier, "Bipolar diffusion encoding with implicit spoiling of undesired coherence pathways," ISMRM Abstract 2011 Nov. 10, 2010, no. 178, p. 1.

[28] H. W. Park, D. J. Kim, and Z. H. Cho, "Gradient reversal technique and its applications to chemical-shift-related NMR imaging," *Magn. Reson. Med.*, vol. 4, no. 6, pp. 526–536, 1987.

[29] T. Feiweier, "Magnetic resonance method and apparatus to determine phase correction parameters," U.S. Patent 20110234221, Sep. 29, 2011.

[30] T. P. Trouard, Y. Sabharwal, M. I. Altbach, and A. F. Gmitro, "Analysis and comparison of motion-correction techniques in diffusion-weighted imaging," *J. Magn. Reson. Imag.*, vol. 6, no. 6, pp. 925–935, 1996.

[31] T. Vercauteren, X. Pennec, A. Perchant, and N. Ayache, "Symmetric log-domain diffeomorphic registration: A demons-based approach," *Med. Image Comput. Comput. Interv.*, vol. 11, pp. 754–761, 2008.

[32] T. Vercauteren, X. Pennec, A. Perchant, and N. Ayache, "Diffeomorphic demons: Efficient non-parametric image registration," *NeuroImage*, vol. 45, no. 1, pp. S61–72, 2009.

[33] H. Wei, M. Viallon, B. Delattre, L. Wang, V. M. Pai, H. Wen, H. Xue, C. Guetter, P. Croisille, and Y. Zhu, "Assessment of cardiac motion effects on the fiber architecture of the human heart in vivo," *IEEE Trans. Med. Imag.*, vol. 32, no. 10, pp. 1928–1938, Oct. 2013.

[34] T. G. Reese, O. Heid, R. M. Weisskoff, and V. J. Wedeen, "Reduction of eddy-current-induced distortion in diffusion MRI using a twice-refocused spin echo," *Magn. Reson. Med.*, vol. 49, no. 1, pp. 177–182, 2003.

[35] G. Pajares and J. M. de la Cruz, "A wavelet-based image fusion tutorial," *Pattern Recognit.*, vol. 37, pp. 1855–1872, 2004.

[36] I. Aganj, C. Lenglet, E. Yacoub, G. Sapiro, and N. Harel, "A 3-D wavelet fusion approach for the reconstruction of isotropic-resolution MR images from orthogonal anisotropic-resolution scans," *Magn. Reson. Med.*, vol. 67, no. 4, pp. 1167–1172, 2012.

[37] P. J. Basser and S. Pajevic, "Statistical artifacts in diffusion tensor MRI (DT-MRI) caused by background noise," *Magn. Reson. Med.*, vol. 44, no. 1, pp. 41–50, 2000.

[38] Y. Yang, D. Park, S. Huang, and N. Rao, "Medical image fusion via an effective wavelet-based approach," *EURASIP J. Adv. Signal Process.*, vol. 1, pp. 1–13, 2010.

[39] J. Tian and C. Li, "Adaptive multi-focus image fusion using a wavelet-based statistical sharpness measure," *Signal Process.*, vol. 92, no. 9, pp. 2137–2146, 2012.

[40] L. Zhang, W. Dong, D. Zhang, and G. Shi, "Two-stage image denoising by principal component analysis with local pixel grouping," *Pattern Recognit.*, vol. 43, no. 4, pp. 1531–1549, 2010.

[41] L. Wang, Y. Zhu, H. Li, W. Liu, and I. E. Magnin, "Multiscale modeling and simulation of the cardiac fiber architecture for DMRI," *IEEE Trans. Biomed. Eng.*, vol. 59, no. 1, pp. 16–19, Jan. 2012.

[42] P. J. Basser, "Inferring microstructural features and the physiological state of tissues from diffusion-weighted images," *NMR Biomed.*, vol. 8, pp. 333–344, 1995.
[43] C. Frindel, M. Robini, J. Schaerer, P. Croisille, and Y. M. Zhu, "A graph-based approach for automatic cardiac tractography," *Magn. Reson. Med.*, vol. 64, no. 1, pp. 1215–1229, 2010.
[44] V. Arsigny, P. Fillard, X. Pennec, and N. Ayache, "Log-euclidean metrics for fast and simple calculus on diffusion tensors," *Magn. Reson. Med.*, vol. 56, no. 2, pp. 411–421, 2006.
[45] D. D. Streeter and W. T. Hanna, "Engineering mechanics for successive states in canine left ventricular myocardium II. Fiber angle and sarcomere length," *Circ. Res.*, vol. 33, no. 6, pp. 656–664, 1973.
[46] A. Aldroubi and P. J. Basser, "Reconstruction of vector and tensor fields from sampled discrete data," in *Contemporary Mathematics*, L. W. Baggett and D. R. Larson, Eds. Providence, RI: AMS, 1999, pp. 1–15.
[47] A. H. Aletras, S. Ding, R. S. Balaban, and H. Wen, "DENSE: Displacement encoding with stimulated echoes in cardiac functional MRI," *J. Magn. Reson.*, vol. 137, no. 1, pp. 247–252, 1999.
[48] N. Toussaint, C. T. Stoeck, T. Sermesant, S. Kozerke, M. Sermesant, and P. G. Batchelor, "In vivo human cardiac fibre architecture estimation using shape-based diffusion tensor processing," *Med. Image Anal.*, vol. 17, no. 8, pp. 1243–1255, 2013.
[49] H. Lombaert, J. Peyrat, L. Fanton, F. Cheriet, H. Delingette, N. Ayache, P. Clarysse, I. Magnin, and P. Croisille, "Variability of the human cardiac laminar structure," *Med. Image Comput. Comput. Assist. Interv.*, vol. 7085, pp. 160–167, 2011.
[50] B. T. Yeo, T. Vercauteren, P. Fillard, J. M. Peyrat, X. Pennec, P. Golland, N. Ayache, and O. Clatz, "DT-REFinD: Diffusion tensor registration with exact finite- strain differential," *IEEE Trans. Med. Imag.*, vol. 28, no. 12, pp. 1914–1928, Dec. 2009.